

Effective interaction analysis of 500 MeV (\vec{p}, p') excitation of low-lying states in $^{40,48}\text{Ca}$, ^{90}Zr , and ^{208}Pb

M. L. Barlett, G. W. Hoffmann, and L. Ray

Department of Physics, The University of Texas at Austin, Austin, Texas 78712

(Received 23 September 1986)

A nonrelativistic distorted wave Born approximation analysis, using a phenomenological effective proton-nucleon interaction to generate both optical and transition potentials, is made of *new* 500 MeV (\vec{p}, p') data for excitation of low-lying states in ^{40}Ca , ^{48}Ca , ^{90}Zr , and ^{208}Pb . The data, differential cross section and analyzing power angular distributions for $5^\circ \leq \theta_{c.m.} \leq 30^\circ$, are well described using this effective interaction. Calculations using the impulse approximation to generate the optical and transition potentials do not adequately describe the data. As a further test of the 500 MeV empirical effective interaction, model-dependent neutron transition densities are deduced for excitations which are expected to be purely isoscalar, such as the first 3^- states of ^{40}Ca and ^{208}Pb . These are found to be qualitatively similar in strength and overall shape to the renormalized ($\times N/Z$) model-independent proton densities determined from analysis of (e, e') data. Model-dependent neutron transition densities are also deduced for other excitations and are in reasonable agreement with results of analyses of other hadron plus nucleus scattering data. These results indicate that the 500 MeV isoscalar effective interaction is better than the free proton-nucleon scattering amplitudes (impulse approximation) as a starting point for analysis of (p, p') data aimed at detailed extraction of neutron transition densities and other nuclear structure information.

I. INTRODUCTION

High quality electron plus nucleus scattering data have enabled reliable determinations of model-independent ground state charge (proton) and excited state charge (proton) transition densities. Unfortunately, the same cannot be said of the matter transition densities (and hence the neutron densities if the proton densities are known) that result from analysis of hadron plus nucleus scattering data. The reason for this uncertainty is the inability to cleanly separate, in the predicted scattering observables, effects due to the hadron-nucleon interaction in the nuclear medium from nuclear structure effects; also, invariably, practical applications of theory make use of models and approximations in the analysis of data.

Recently, however, a phenomenological 500 MeV effective interaction¹ (EI) was obtained for a folding model of the optical potential for use in the Schrödinger equation. This interaction led to good descriptions of 500 MeV $\vec{p} + \text{nucleus}$ (\vec{p}, A) elastic scattering cross section, analyzing power, and spin-rotation data.²⁻⁴ In addition, neutron-proton root-mean-square radius differences, Δr_{np} , obtained in the analysis agreed with theoretical expectations (to within the quoted uncertainties) for the nuclei studied ($^{40,48}\text{Ca}$, ^{90}Zr , ^{208}Pb). Such was not the case when the first order microscopic optical potential as prescribed in the impulse-approximation (IA) by the Kerman-McManus-Thaler⁵ (KMT) formalism was used.²

In this work we test the usefulness of the effective interaction of Ref. 1 for the case of inelastic scattering; a distorted wave Born approximation (DWBA) analysis is made of 500 MeV (\vec{p}, p') data for excitation of collective states in nuclei $^{40,48}\text{Ca}$, ^{90}Zr , and ^{208}Pb . The ^{90}Zr and

^{208}Pb data reported herein are new, whereas the $^{40,48}\text{Ca}$ data are similar to those reported in Ref. 6, but obtained from an independent data reduction. We find that use of the effective interaction leads to good descriptions of the data and to deduced model-dependent neutron transition densities whose overall strengths and general surface geometries are reasonable (i.e., the deduced model-dependent neutron transition densities for isoscalar transitions are approximately the same as the renormalized ($\times N/Z$) known proton transition densities). Calculations made using the IA to generate the optical and transition potentials do not adequately describe the data. These results demonstrate that the EI of Ref. 1 provides the best isoscalar, spin-independent and spin-orbit two-body interaction presently available for use in careful nonrelativistic microscopic analyses of these and other elastic and inelastic scattering data at 500 MeV. The results are also compared with those obtained from analyses of other data (different probes and/or bombarding energies).

II. EXPERIMENT

The 500 MeV (\vec{p}, p') data analyzed in this work were taken using the high resolution spectrometer (HRS) at the Los Alamos Clinton P. Anderson Meson Physics Facility (LAMPF) during the elastic scattering experiment.² Results of an independent data reduction and macroscopic analysis for ^{40}Ca and ^{48}Ca can be found in the literature.⁶ The ^{90}Zr and ^{208}Pb data are new.

The 500 MeV (\vec{p}, p') angle-sorted missing-mass spectra were analyzed using the lineshape fitting program LOAF.⁷ Angular distributions of differential cross section and analyzing power were obtained for excitation of the 3_1^-

(3.74 MeV) and 2_1^+ (3.90 MeV) states of ^{40}Ca , the 2_1^+ (3.83 MeV) and 3_1^- (4.51 MeV) states of ^{48}Ca , the 2_1^+ (2.19 MeV), 3_1^- (2.75 MeV), and 2_2^+ (3.31 MeV) states of ^{90}Zr , and the 3_1^- (2.61 MeV) and 5_1^- (3.20 MeV) states of ^{208}Pb . The uncertainty in the absolute normalization of the differential cross section data is $\sim \pm 5\%$.² The data, together with the results of the analysis to be discussed, are shown in Figs. 1, 5, 7, 8, 11, 13, 14, 16, and 18. The errors shown are statistical only. The gaps in some of the angular distributions correspond to angular regions where contaminant peaks could not be stripped from the yields of interest. Other details of the experiment are as stated in Refs. 2 and 6.

III. THEORETICAL MODEL AND ANALYSIS

A. Elastic scattering and optical potentials

Spin-independent and spin-orbit proton plus nucleus (pA) optical potentials for use in the Schrödinger equation (with relativistic kinematics) were generated by folding the effective, two-body interaction no. 2 of Ref. 1 with experimental point-proton densities⁸ and model¹ point-neutron densities. The parameters of the neutron densities were varied to optimize the fits to the elastic cross section data.²

Similarly, impulse-approximation optical potentials were generated by folding the spin-independent and spin-orbit free proton plus nucleon (pN) amplitudes⁹ in the Breit frame¹⁰ with the experimental point-proton⁸ and model¹ neutron densities. Again the neutron density parameters were varied to optimize the fits to the elastic cross section data.

The folding model for the proton-nucleus elastic scattering optical potential used here is explained in detail in Ref. 1. The components of the effective isoscalar interaction no. 2 from $q=0-2.5\text{ fm}^{-1}$ are given in Table II of Ref. 1; comparisons between the effective and IA isoscalar amplitudes are shown in Fig. 5 of Ref. 1. For the IA optical potential, Arndt⁹ nucleon-nucleon scattering amplitudes were converted into two-body, on-shell t matrices in the proton-nucleus Breit kinematic frame as explained in Ref. 10. These two-body t matrices were folded with proton and neutron densities to obtain the optical potential as in Ref. 1. For all calculations presented here which use the effective isoscalar interaction, the isovector portions of the optical potential and inelastic transition

potential (see Sec. III B) were obtained using the isovector value of the two-body IA interaction.

The results of the analysis are essentially the same as shown in Figs. 1–3 (cross section, analyzing power, and spin-rotation data) of Ref. 1. The IA fits to the data are similar to those shown in Figs. 1 and 2 of Ref. 2 (cross sections and analyzing powers) and Fig. 2 of Ref. 3 (analyzing powers and spin rotation); the IA fits are, of course, inferior to those obtained with the EI. The resulting ground state neutron-proton root-mean-square radius differences, Δr_{np} , are the same as given in Table III of Ref. 1 with two exceptions: (1) the neutron density for ^{40}Ca was varied, resulting in values of $\Delta r_{np}^{\text{EI}} = -0.10\text{ fm}$ and $\Delta r_{np}^{\text{IA}} = -0.37\text{ fm}$ for the EI and IA analysis, respectively, and (2) the neutron density of ^{90}Zr was reevaluated in the EI analysis since a new point-proton density from recent⁸ electron scattering work was available. The refit of the ^{90}Zr data resulted in $\Delta r_{np}^{\text{EI}} = 0.04\text{ fm}$, compared to a value of 0.05 fm obtained in Ref. 1.

B. DWBA transition potentials and method of analysis

500 MeV (\vec{p}, p') inelastic differential cross section and analyzing power predictions were obtained in the distorted wave Born approximation^{5,11} (DWBA) using the computer code DWBA-70.¹² DWBA-70 uses relativistic kinematics but treats the scattering dynamics nonrelativistically. Transition potentials for the DWBA calculations were generated using the code ALLWORLD.¹³ The optical potentials discussed in Sec. IIIA were used to generate the distorted waves.

The transition amplitude for excitation of the nucleus from its ground state $|\Phi_{g.s.}\rangle$ to the n th excited state $|\Phi_n\rangle$ is given by⁵

$$T_{g.s. \rightarrow n} = \langle \phi_n^{(-)} | \langle \Phi_n | \mathcal{W} | \Phi_{g.s.} \rangle | \Psi_0^{(+)} \rangle, \quad (1)$$

where $\Psi_0^{(+)}$ is the incident distorted wave in the elastic channel, $\phi_n^{(-)}$ is the final state distorted wave, and \mathcal{W} is the transition potential operator.

The transition matrix element contains both spin-independent and deformed spin-orbit parts. It is given by

$$\langle \Phi_n | \mathcal{W} | \Phi_{g.s.} \rangle = F_l(r) Y_{lm}^*(\hat{r}) + F_{lm}^{\text{DSO}}(\mathbf{r}), \quad (2a)$$

where¹⁴

$$F_l(r) = 4\pi K \sum_{i=p,n} \int_0^\infty j_l(qr) a_{pi}(q) \tilde{\rho}_{i,l}^{\text{tran}}(q) q^2 dq, \quad (2b)$$

and

$$F_{lm}^{\text{DSO}}(\mathbf{r}) = -iK\sigma \cdot \left\{ \nabla \left[\sum_{i=p,n} 4\pi \int_0^\infty j_l(qr) \tilde{C}_{pi}(q) \tilde{\rho}_{i,l}^{\text{tran}}(q) q^2 dq Y_{lm}^*(\hat{r}) \right] \times \frac{\nabla}{i} \right\}. \quad (2c)$$

The latter term corresponds to the full Thomas deformed spin-orbit potential for collective excitations.¹⁵ In Eqs. (2b) and (2c) p and n denote proton and neutron, respectively, and

$$K = - \frac{(\hbar c)^2 \kappa_L \eta}{(2\pi)^2 E_L \kappa_0},$$

where κ_L , E_L , and κ_0 are the relativistic laboratory projectile wave number, total relativistic laboratory energy, and proton-nucleon center-of-momentum system wave number, respectively. The kinematic factor η is defined in Ref. 5. The proton-nucleon scattering amplitude is assumed to be of the form

$$f_{pi} = a_{pi}(q) + c_{pi}(q) \sigma \cdot \hat{n} + \dots,$$

where $i =$ proton (p) or neutron (n) and the omitted terms depend on target nucleon spin. The spin-orbit amplitude appearing in Eq. (2c) is given by

$$\tilde{C}_{pi}(q) = \frac{c_{pi}(q)}{|\mathbf{k}_N \times \mathbf{k}'_N|},$$

where \mathbf{k}_N (\mathbf{k}'_N) is the initial (final) proton-nucleus center-of-momentum system wave number. The transition density form factors in momentum space are given by

$$\tilde{\rho}_{i,l}^{\text{tran}}(q) = 4\pi \int_0^\infty j_l(qr) \rho_{i,l}^{\text{tran}}(r) r^2 dr,$$

where $\rho_{i,l}^{\text{tran}}(r)$ is the proton or neutron transition density in coordinate space as discussed below. Both the free and the effective pN scattering amplitudes, together with the appropriate transition densities, were used to generate the transition potentials (the IA or EI transition potentials, respectively).

The point-proton transition densities were unfolded from charge transition densities obtained from (e, e') experiments. Model-dependent neutron transition densities were taken as derivatives of two parameter Fermi functions:

$$\rho_{n,l}^{\text{tran}}(r) = \frac{d}{dr} f(r), \quad (3)$$

where

$$f(r) = \xi_l \frac{1}{1 + \exp[(r - c)/z]}. \quad (4)$$

The strength (ξ_l), range (c), and diffuseness (z) of the two parameter Fermi function were varied for each transition to optimize the fits to the cross section data. We found that analyzing power predictions for (\bar{p}, p') were primarily sensitive to the spin-dependent effective interaction and were not critically sensitive to $\rho_{n,l}^{\text{tran}}(r)$ (see Table I in Ref. 14); therefore the analyzing power data were not included

in the fitting procedure. Table I gives the best fit parameters obtained from the analysis discussed in the next section. The multipole moment of the neutron transition density,

$$M_{n,l}(El) = \int_0^\infty r^{2+l} \rho_{n,l}^{\text{tran}}(r) dr, \quad (5)$$

was determined for each best fit density. The corresponding moment of the proton density was also computed so that multipole moment ratios could be obtained. Ratios of the reduced multipole moments, defined

$$\tilde{M}_{n,l}(El) = (1/N) M_{n,l}(El)$$

and

$$\tilde{M}_{p,l}(El) = (1/Z) M_{p,l}(El),$$

were also computed. Table II summarizes the multipole moments and moment ratios that resulted from the analysis discussed in the next section.

All of the inelastic differential cross sections studied here peak at momentum transfers well inside 2.5 fm^{-1} . Therefore the effective interaction model of Ref. 1 is applicable to analyses of the angular distributions and subsequent studies of the overall strength and qualitative features of the surface geometry of the neutron transition densities. Analyses aimed at determining possible structure in the nuclear interior region of the transition densities would require, among other things, an effective interaction accurate to larger momentum transfer. Also, for the strong, collective excitations studied here, the isovector portion of the *transition potential* is only a few percent, relative to the isoscalar term, and cannot significantly affect our conclusions regarding the utility of the isoscalar effective interaction or the qualitative surface features of the neutron transition densities.

TABLE I. Parameters of deduced neutron transition densities [see Eqs. (3) and (4) of text].

Nucleus	J^π	E (MeV)	ξ_l (n/fm ²)	c (fm)	z (fm)	Comment
⁴⁰ Ca	3_1^-	3.74	0.022 20	3.3771	0.5632	EI
			0.038 60	3.3689	0.3928	IA
			0.028 51	2.9198	0.6904	SE
⁴⁸ Ca	2_1^+	3.90	0.007 94	3.3475	0.6346	EI
			0.014 01	3.9614	0.5423	EI
⁹⁰ Zr	3_1^-	4.51	0.014 17	3.5830	0.5903	EI
			0.011 74	4.5708	0.6046	EI
⁹⁰ Zr	2_2^+	2.19	0.005 58	4.6861	0.5937	EI
			0.016 85	4.5809	0.6203	EI
			0.012 67	6.4939	0.6962	EI
²⁰⁸ Pb	3_1^-	2.61	0.014 95	6.5137	0.5904	IA
			0.004 29	6.5693	0.6997	EI
			0.004 29	6.5693	0.6997	EI

TABLE II. Deduced neutron multipole moments and neutron/proton multipole moment ratios.

Nucleus	J^π	E (MeV)	M_n (fm ^l)	M_n/M_p	\tilde{M}_n/\tilde{M}_p	Reference	Comments
40Ca	3_1^-	3.74	45.6	0.90	0.90	this work	EI
			39.2	0.78	0.78	this work	IA
			57.8	1.15	1.15	this work	SE
				0.99	0.99	18	800 MeV (p,p')
2_1^+	3.90	4.44	0.98	0.98	this work	EI	
			1.20	1.20	18	800 MeV (p,p')	
48Ca	2_1^+	3.83	10.3	2.55	1.82	this work	EI
				2.63	1.88	40	($\pi^\pm, \pi^{\pm'}$)
3_1^-	4.51	40.2	1.26	0.90	this work	EI	
			1.17	0.84	40	($\pi^\pm, \pi^{\pm'}$)	
90Zr	2_1^+	2.19	16.8	1.47	1.18	this work	EI
				1.12	0.90	18	800 MeV (p,p')
3_1^-	2.75	141	1.31	1.05	this work	EI	
			1.06	0.85	18	800 MeV (p,p')	
208Pb	3_1^-	2.61	568	1.88	1.22	this work	EI
			531	1.76	1.14	this work	IA
				1.72	1.12	18	800 MeV (p,p')
			519	1.72	1.12	14	800 MeV (p,p')
	5_1^-	3.20	12 348	1.94	1.26	this work	EI
			1.81	1.18	18	800 MeV (p,p')	

IV. RESULTS OF ANALYSIS

Before discussing the results of analysis, we emphasize that it is not our intention here to extract detailed neutron transition densities. Such analyses (1) would require a well understood interaction and dynamical model for the proton-nucleus system, (2) should account for effects due to correlations, multistep processes, off-shell dependences, exchange processes, medium modifications, etc., and (3) should utilize model-independent forms⁸ for the transition densities. Instead, our intention is to explore at least a portion of the first item in the aforementioned list by determining if analyses using the EI of Ref. 1 can obtain good fits to (p,p') angular distributions and deduce $\rho_{n,l}^{\text{tran}}(r)$ which have overall strengths and surface geometries which are reasonable.

A. ⁴⁰Ca

Since ⁴⁰Ca is self-conjugate and its ground state is essentially closed shell, many of the low-lying states are expected to be isoscalar collective excitations. We therefore expect the deduced model-dependent neutron transition densities of these states to be similar to the proton transition densities. Hence the ⁴⁰Ca analysis can serve as an important test of the model.

The structure of the 3_1^- (3.74 MeV) state has been studied extensively via electron,^{16,17} proton,¹⁸⁻²¹ and pion^{22,23} scattering, and also with the use of other probes and methods.²⁴ Deduced nuclear structure information from

these works¹⁶⁻²³ indicates that the 3_1^- state is predominantly isoscalar and that spin-flip contributions to its excitation are small. In particular, the charge transition density¹⁶ is characteristically collective.

Two calculations were made for 500 MeV ⁴⁰Ca(\bar{p}, p')⁴⁰Ca(3_1^-). The first used the EI of Ref. 1; the second used free pN scattering amplitudes (IA) from a recent phase shift analysis solution.⁹ For both calculations the optical and transition potentials were constructed as described in Sec. III, and the parameters of each model neutron transition density were varied to obtain the best fit ($|\chi|^2$ optimization, see Table I) to the cross section angular distribution data. Shown in Fig. 1 are the resulting fits. The corresponding predictions for the analyzing power (A_y) are also compared with the data. As seen in Fig. 1, the cross section data are well described using either interaction. However, the best description of the A_y data is obtained using the EI. Similar differences were seen between IA and EI descriptions²⁵ of spin-rotation (D_{ij}) data²⁶ for this (\bar{p}, p') excitation.

The model neutron transition densities deduced from the analysis are shown in Fig. 2 (also see Table I), where they are compared with the point-proton transition density¹⁶ (statistical errors are quite small and are not shown). The dashed-dotted density in Fig. 2 is discussed later. The model neutron transition densities differ substantially, both in geometry and magnitude. That obtained from the EI analysis (solid curve) is similar in magnitude and shape to the empirical point-proton density (dotted curve),

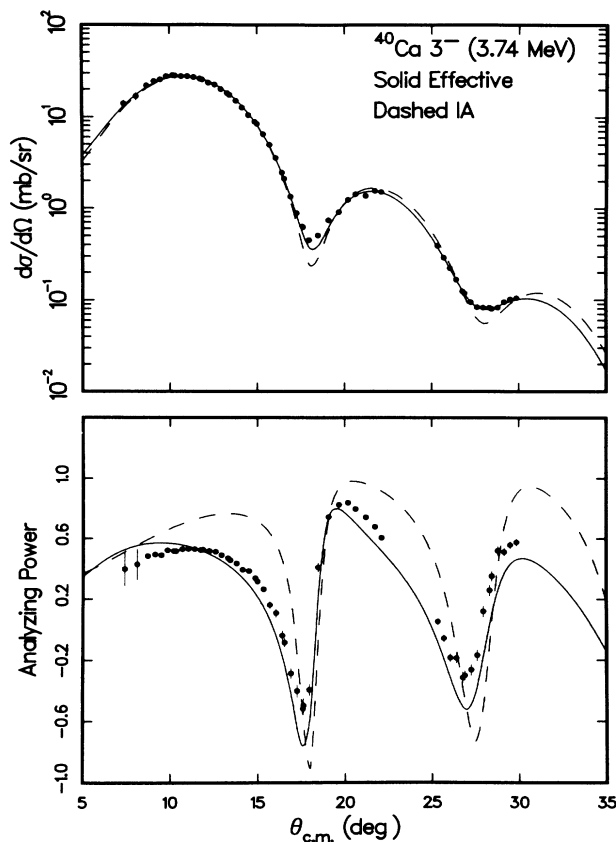


FIG. 1. 500 MeV $^{40}\text{Ca}(\bar{p}, p')^{40}\text{Ca}(3_1^-, 3.74 \text{ MeV})$ differential cross section and analyzing power data are compared with results of DWBA analysis obtained using the effective interaction (solid curve) and the impulse approximation (dashed curve) to generate the optical and transition potentials.

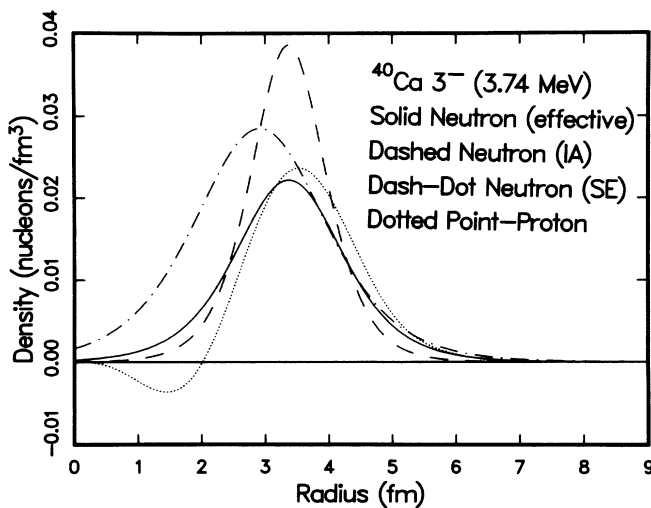


FIG. 2. Model neutron transition densities for the 3_1^- state of ^{40}Ca obtained from the effective interaction analysis (solid curve), the impulse-approximation analysis (dashed curve), and the Schrödinger equivalent analysis (dashed-dotted curve) are compared with the point-proton transition density (dotted curve) unfolded from (e, e') results of Ref. 16.

although a small difference in radial peak positions is evident ($\sim 0.25 \text{ fm}$); this difference is similar to that observed when comparing the half-density radii of proton and deduced neutron ground state densities.¹ The corresponding multipole moments and neutron/proton multipole moment ratios are presented in Table II. The ratio of 0.9 obtained from the EI analysis is in general agreement with other analyses which indicate that the 3_1^- excitation is predominantly isoscalar. The ratio 0.78 from the IA analysis, if taken literally, would suggest some isovector contribution to the excitation.²⁷ Since this contradicts results from numerous other structure studies,¹⁸⁻²³ we conclude that the effective interaction, rather than the impulse approximation, should be used in analyses aimed toward deducing accurate nuclear structure information. Detailed discussions of errors associated with deduced structure information such as radial shapes and multipole moments may be found elsewhere^{14,28,29} and indicate that 500 MeV (p, p') studies should give reasonably accurate nuclear structure information for low-lying collective states. A recent estimate¹⁴ which includes statistical and model dependence errors gave an uncertainty in the deduced multipole moments of $\sim \pm 10\%$ for data of the quality presented here. Model independent analyses²⁹ of intermediate energy (p, p') data for low-lying collective states indicate that typical statistical uncertainties in the nuclear surface region of $\rho_{n,l}^{\text{tran}}(r)$ are much less than the differences between the model neutron transition densities shown in Fig. 2 by the solid and dashed curves. Statistical uncertainty in the fit to high quality data like those presented here is not a significant factor in choosing the best interaction model.

An indication of the sensitivity of the (p, p') differential cross section predictions to the model neutron transition densities is provided in Fig. 3, which shows results of EI calculations using (1) the best fit model neutron transition

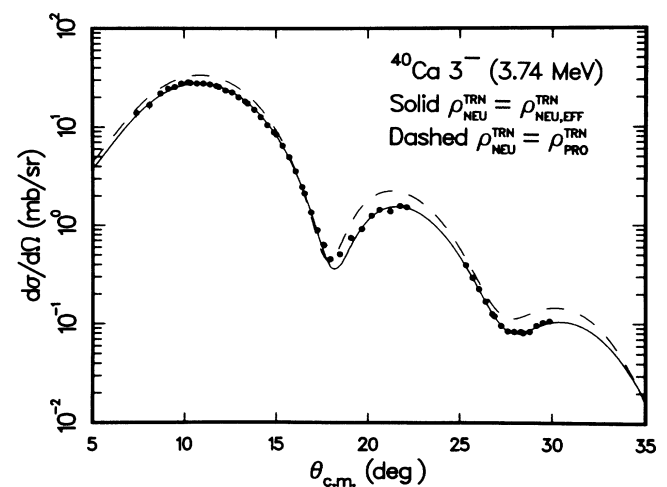


FIG. 3. DWBA cross section results for 500 MeV $^{40}\text{Ca}(\bar{p}, p')^{40}\text{Ca}(3_1^-, 3.74 \text{ MeV})$ obtained using the neutron transition density from the effective interaction fit (solid curve, same as the solid curve in Fig. 1) and a neutron transition density equal to the point-proton transition density (dashed curve).

density (solid curve of Fig. 2), and (2) a model neutron transition density equal to the proton transition density (dotted curve of Fig. 2). The differences between the two results indicate the level of sensitivity to the variations in the model neutron transition densities indicated in Fig. 2 (predominantly the differences in the surface regions). Studies show that forward angle (p,p') angular distribution predictions are insensitive to interior structure in the matter transition densities.³⁰ The present analysis is not relevant for detailed structure studies for radii somewhat less than the half-density radius. Furthermore, because of the r^{2+l} factor in Eq. (5), multipole moments are generally unaffected by interior structure in the transition densities.

Recent successful³¹⁻³⁷ descriptions of the elastic data obtained using the Dirac equation provide a means for investigating the effect that optical potential ambiguities could have in determinations of neutron transition density information. These relativistic approaches³¹⁻³⁷ use Dirac phenomenology or the relativistic impulse approximation (RIA) and give Schrödinger equivalent³⁸ (SE) optical potentials (i.e., optical potentials for use in the Schrödinger equation) which differ substantially in shape and magnitude from nonrelativistic KMT optical potentials in the IA and from the EI optical potentials discussed here.

We investigated the effect of this particular optical potential ambiguity on deduced transition density information by making an analysis of the 3_1^- data using a SE optical potential obtained from the 500 MeV $p+^{40}\text{Ca}$ RIA potential of Ref. 37. This potential led to good descriptions of the elastic cross section, analyzing power, and spin-rotation data; the fits were equivalent to those obtained with the effective interaction and folding model.¹ A two-body effective interaction corresponding to the SE optical potential does not exist; therefore for this calculation we cannot maintain consistency between the effective two-body information used to describe the elastic and inelastic channels as we have done for the EI and IA analyses. The transition potential for the initial DWBA calculation was that used to produce the solid curve of Fig. 1. The dashed curves of Fig. 4 are the results, where the solid curves in Fig. 4 are the same as the solid curves in Fig. 1. The difference between the dashed and solid curves displays directly the effects of optical potential ambiguities. This new cross section prediction does not quantitatively describe the shape and magnitude of the angular distribution. The parameters of the model neutron transition density were then varied to recover the fit. The results are indicated by the dashed-dotted curves of Fig. 4; we see that the EI fit is better than the SE fit for the entire region beyond the first maximum. The model neutron density so obtained is shown as the dashed-dotted curve of Fig. 2. This model density does not compare as well with the proton density as does the EI result. The SE multipole moment of 57.8 fm^3 is 27% larger than the result of the EI analysis. A consistent relativistic description for both the elastic and inelastic channels might result in a more reasonable fit to the data and a model neutron transition density which is in better agreement with the proton transition density. These results do indicate however that comparable descriptions of elastic data will

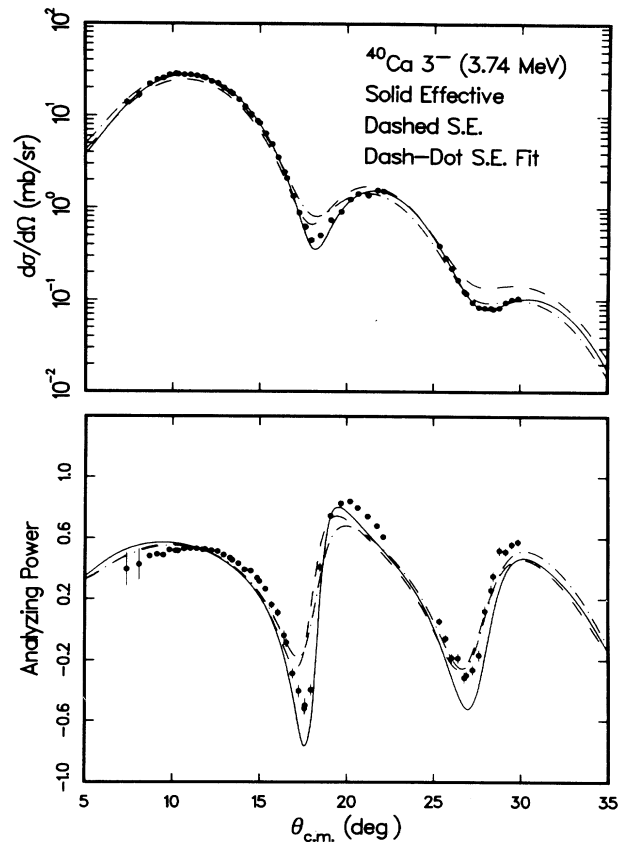


FIG. 4. DWBA cross section and analyzing power results for 500 MeV $^{40}\text{Ca}(\bar{p},p)^{40}\text{Ca}(3_1^-, 3.74 \text{ MeV})$. The solid curve is the same as the solid curve of Fig. 1. The dashed curve is the result obtained using a Schrödinger equivalent optical potential from Ref. 37, but the same transition potential used for generating the solid curve. The dashed-dotted curve is the result obtained using the Schrödinger equivalent optical potential and varying the neutron transition density parameters to obtain the best fit to the cross section data.

not automatically lead to comparable descriptions of (p,p') collective state inelastic data and comparable deduced structure information and indicate a potential source of error for careful analyses aimed at deducing neutron transition densities. Extensions of studies of this type are clearly necessary.

The 2_1^+ (3.90 MeV) data were also analyzed using the effective interaction model. The good fit to the cross section is shown in Fig. 5; the predicted analyzing power also compares well with the data. The fitted model neutron transition density is compared with the point-proton transition density¹⁶ in Fig. 6; the multipole moments and neutron/proton multipole moment ratios are given in Table II. The similarity between the proton and model neutron transition density multipole moments and surface geometries is a reasonable result since one would expect this excitation to be isoscalar.

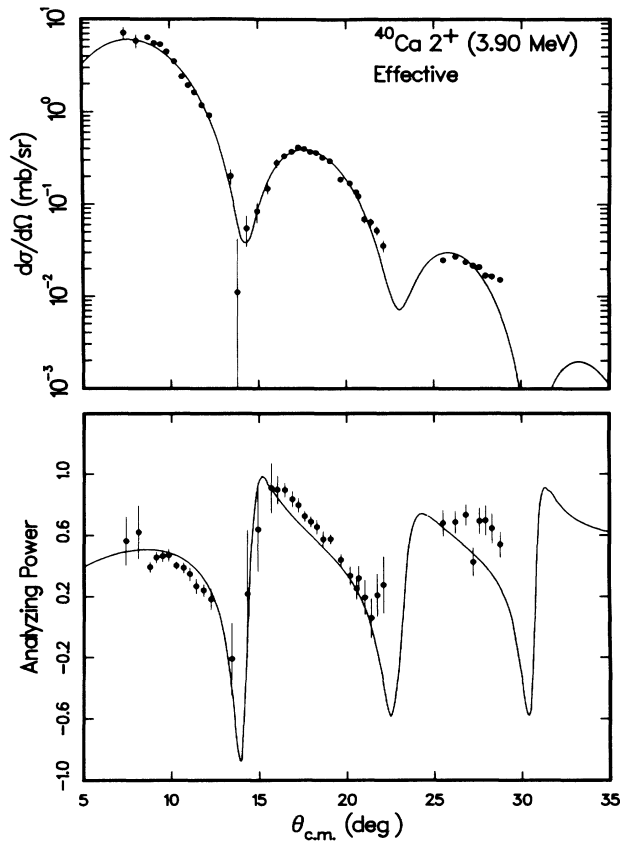


FIG. 5. 500 MeV $^{40}\text{Ca}(\bar{p}, p')^{40}\text{Ca}(2_1^+, 3.90 \text{ MeV})$ differential cross section and analyzing power data are compared with results of DWBA analysis obtained using the effective interaction.

B. ^{48}Ca

Calculations based on the effective interaction were made for (\bar{p}, p') excitation of the low-lying 2_1^+ (3.83 MeV) and 3_1^- (4.51 MeV) states in ^{48}Ca . Point-proton

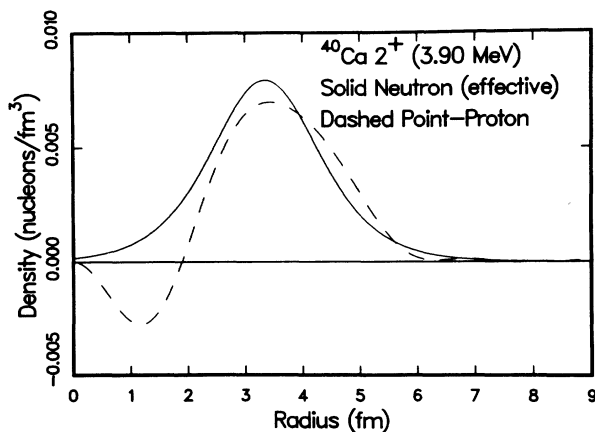


FIG. 6. The model neutron transition density for the 2_1^+ state of ^{40}Ca obtained from the effective interaction analysis (solid curve) is compared with the point-proton transition density (dashed curve) unfolded from the (e, e') results of Ref. 16.

transition densities for both states were generated from results of a recent model-independent analysis³⁹ of (e, e') data. Model neutron transition densities were adjusted to obtain the optimum descriptions of the differential cross section data. The resulting fits, as well as the predicted analyzing powers, are shown in Figs. 7 and 8. Good descriptions of the data are obtained for both excitations using the effective interaction. Figures 9 and 10 compare the fitted, model-dependent neutron transition densities with the renormalized ($\times N/Z$) proton densities. The multipole moments of the former and neutron/proton multipole moment ratios are given in Table II. The 2_1^+ model-dependent neutron transition density peaks at a slightly larger radius, and has a larger surface contribution, than does the proton transition density. The isovector nature of this state (also note the multipole moment ratio) is consistent with conclusions of previous studies.^{19,40} For the 3_1^- state the proton and model neutron transition densities both peak at approximately the same radial position; however, the model neutron transition density exhibits a larger tail contribution than does the proton transition density, whereas the former is reduced in the surface region. The multipole moment of the fitted 3_1^- model neutron transition density is also in good agreement with previous studies.⁴⁰

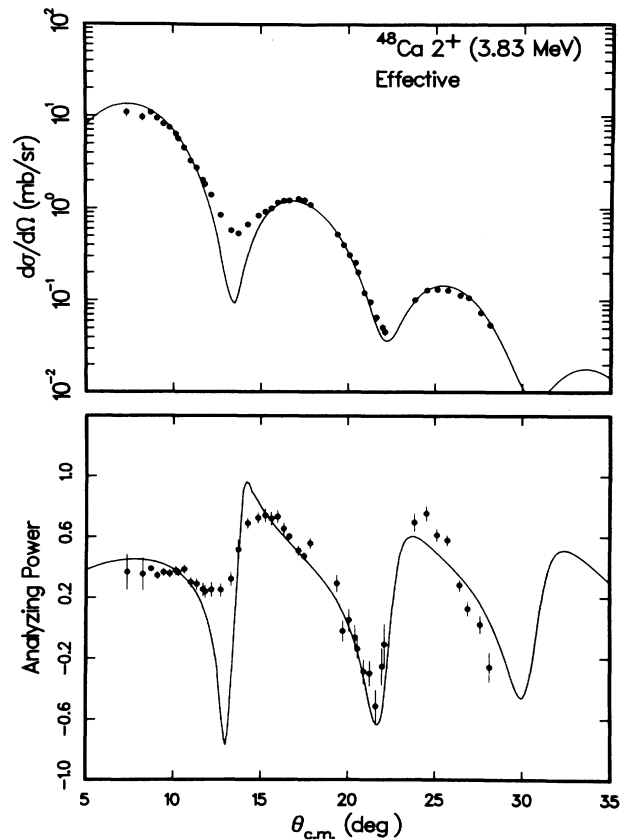


FIG. 7. Same as Fig. 5, except for the 2_1^+ (3.83 MeV) state of ^{48}Ca .

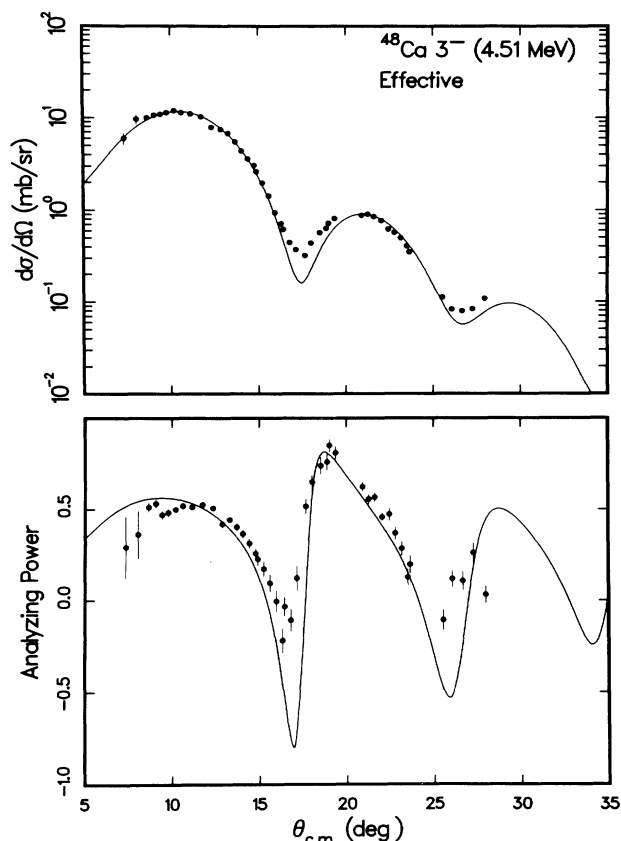


FIG. 8. Same as Fig. 5, except for the 3_1^- (4.51 MeV) state of ^{48}Ca .

C. ^{90}Zr

The 2_1^+ (2.19 MeV) state in ^{90}Zr has been the subject of several nuclear structure studies.^{18,41-43} The radial shape of the point-proton transition density, unfolded from a model-independent analysis of (e,e') data,⁸ is characteristic of a collective state: a symmetric single-lobed density

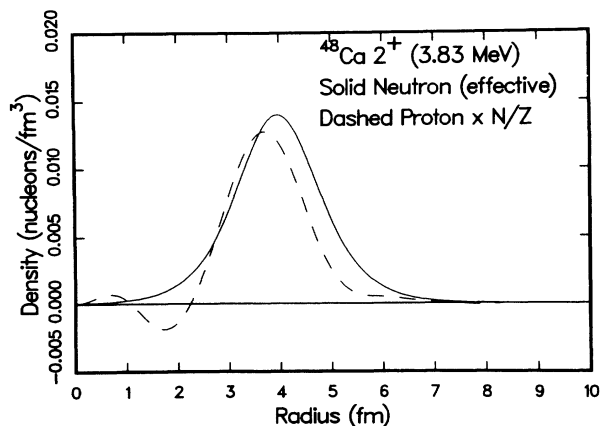


FIG. 9. The model neutron transition density for the 2_1^+ state of ^{48}Ca obtained from the effective interaction analysis (solid curve) is compared with the renormalized $(\times N/Z)$ point-proton transition density (dashed curve) unfolded from (e,e') results of Ref. 39.

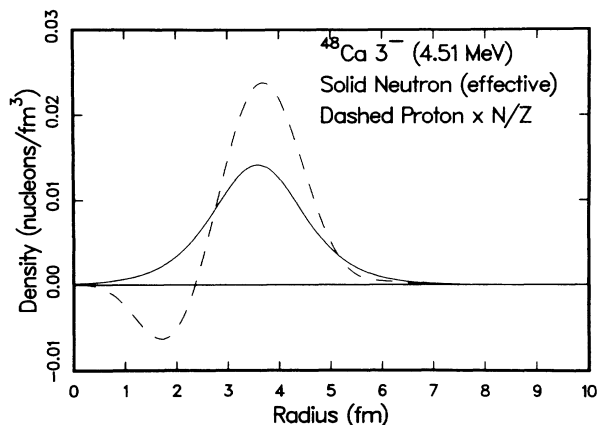


FIG. 10. Same as Fig. 9, except for the 3_1^- state of ^{48}Ca and a point-proton density unfolded from results of Ref. 39.

peaked at the nuclear surface. The EI fit to the differential cross section data, as well as the predicted analyzing power angular distribution, are shown in Fig. 11. The descriptions of both the cross section and analyzing power data are satisfactory. The deduced model-dependent neutron transition density is compared with the renormalized $(\times N/Z)$ proton transition density in Fig. 12; they are seen to be very similar in overall strength and surface geometry. The multipole moment ratio obtained here is

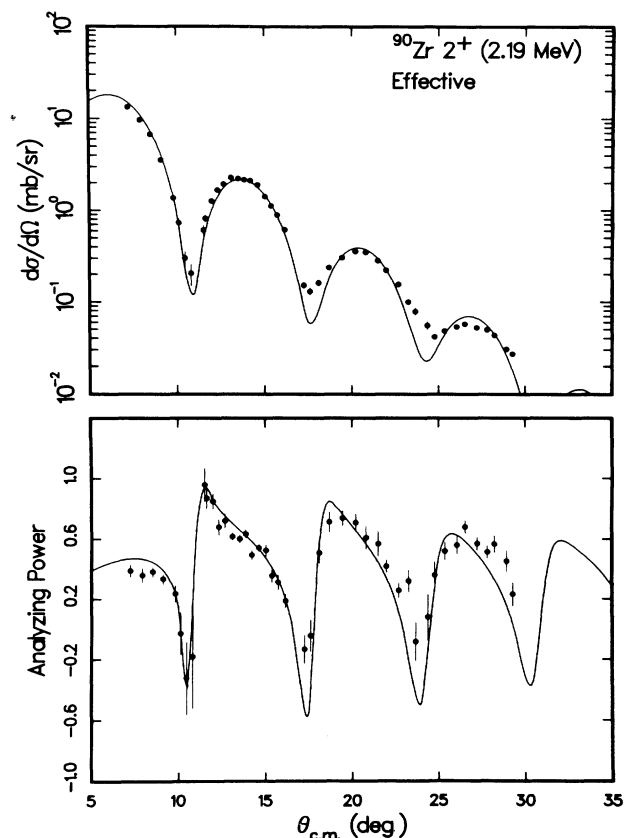


FIG. 11. Same as Fig. 5, except for the 2_1^+ (2.19 MeV) state of ^{90}Zr .

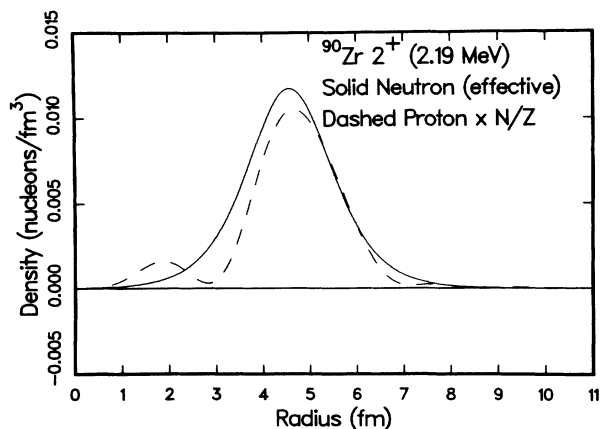


FIG. 12. Same as Fig. 9, except for the 2_1^+ state of ^{90}Zr and a point-proton density unfolded from results of Ref. 8.

somewhat larger than that found at 800 MeV.¹⁸

The 2_2^+ (3.31 MeV) data were also analyzed using the effective interaction model. Electron scattering works^{8,43} give a radial shape for the charge transition density which is substantially different from that of the 2_1^+ state: a considerable portion of the transition density occurs in the nuclear interior. In addition, a sizable transverse elec-

tromagnetic form factor is seen for the 2_2^+ excitation in electron scattering experiments.⁸ Thus, spin-flip processes may play an important role in the (p, p') excitation of this state. Because of these complications in the nuclear structure and reaction mechanism, our model is not well suited for analysis of this state. We have, however, fitted the 2_2^+ cross section data as shown in Fig. 13, which also displays the corresponding analyzing power prediction. The agreement between the differential cross section and analyzing power predictions and the data is comparable to that obtained in the 2_1^+ case. We point out that a good description of the data can be obtained with the simple, surface peaked model for $\rho_{n,l}^{\text{tran}}(r)$.

Finally, the 3_1^- (2.75 MeV) cross section data were analyzed using the effective interaction model. The cross section fit and analyzing power prediction compare well with the data as shown in Fig. 14. The deduced neutron and renormalized proton transition densities are similar as shown in Fig. 15. The multipole moment ratio obtained here is also somewhat larger than that found at 800 MeV (Ref. 18), as is the case for the 2_1^+ state.

D. ^{208}Pb

The large neutron excess of ^{208}Pb makes the 3_1^- (2.61 MeV) and 5_1^- (3.20 MeV) data interesting for analysis. Both EI and IA calculations were made for the 3_1^- data.

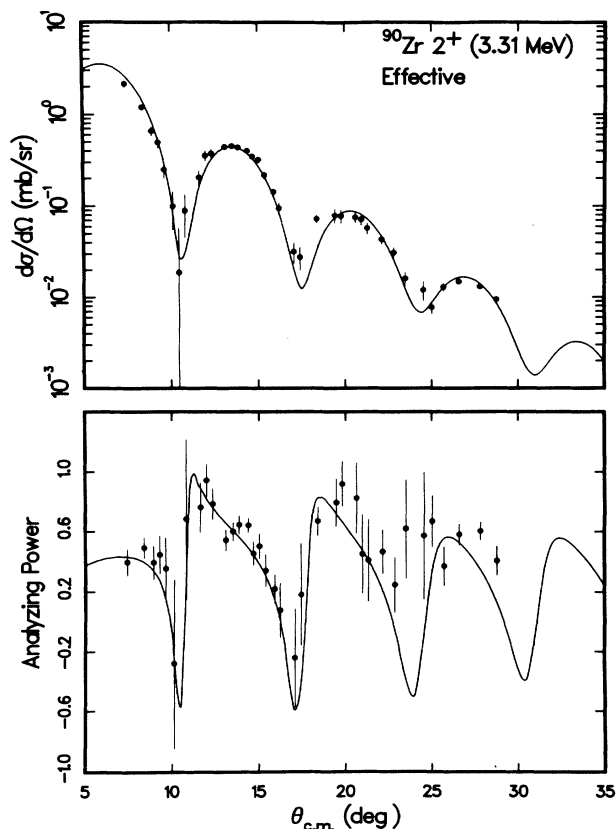


FIG. 13. Same as Fig. 5, except for the 2_2^+ (3.31 MeV) state of ^{90}Zr .

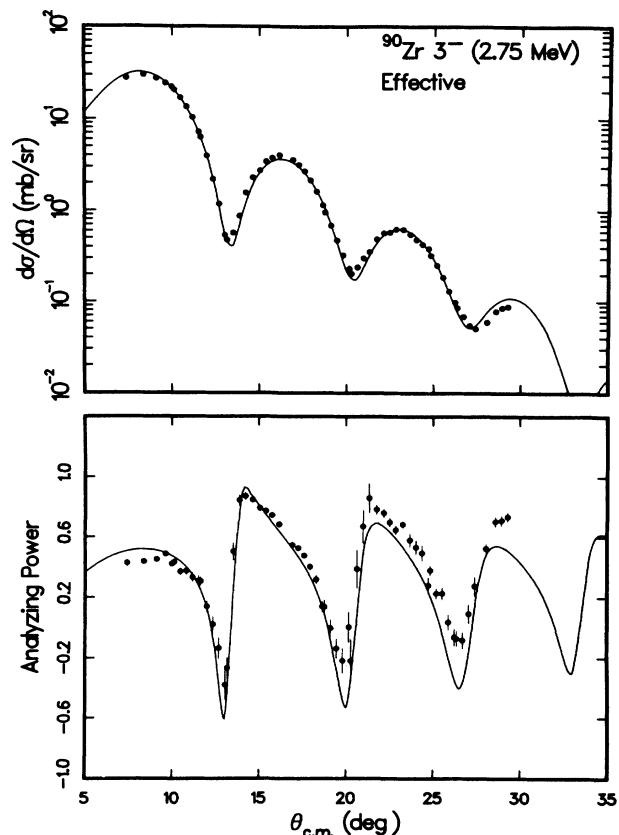


FIG. 14. Same as Fig. 5, except for the 3_1^- (2.75 MeV) state of ^{90}Zr .

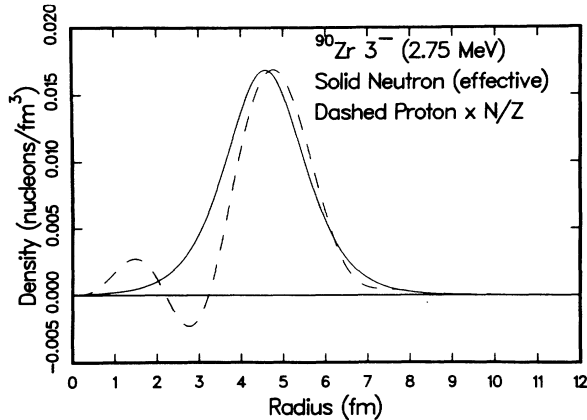


FIG. 15. Same as Fig. 9, except for the 3_1^- state of ^{90}Zr and a point-proton density unfolded from results of Ref. 8.

The point-proton density was unfolded from the charge density determined via analysis of electron scattering data.⁴⁴ The fits to the cross section data and the analyzing power predictions are shown in Fig. 16, where it is seen that the best description of the data is obtained with the EI model. The minima in the IA cross section predictions are much too deep. The two analyzing power predictions differ substantially. The EI calculation gives a good description of the data at forward angles ($\theta_{c.m.} \leq 20^\circ$), whereas the IA calculation provides a very poor representation of the data at forward angles. Both results are only in qualitative agreement with the data at the larger angles. However, the data clearly show a preference for the effective interaction model.

The deduced model-dependent neutron transition densities are compared with the renormalized proton transition density in Fig. 17. Both EI and IA multipole moment ratios (Table II) are consistent with a relatively small isovector component for this state. The IA result is in good agreement with previously determined values,^{14,18} the EI result suggests a slightly larger isovector contribution than do the previous studies.

Previous works⁴⁴⁻⁴⁸ have shown that the 5_1^- (3.2 MeV) state is not purely collective and that a transition current density is required to successfully describe (e, e') data. However, the transition current is important only at relatively large momentum transfer ($q > 2.5 \text{ fm}^{-1}$), suggesting that the spin-dependent parts of the proton-nucleon interaction (other than the spin-orbit interaction) should be relatively unimportant for the analysis of (p, p') data for $q < 2.5 \text{ fm}^{-1}$.

The effective interaction fit to the 5_1^- cross section data is shown in Fig. 18. Also shown is the corresponding analyzing power prediction. The deduced model-dependent neutron transition density is compared with the renormalized proton density⁴⁴ in Fig. 19. The scaled proton transition density and the model neutron transition density are reasonably similar in the surface and tail regions. The multipole moments and moment ratios given in Table II are comparable to that obtained for the 3_1^- state and are in qualitative agreement with results of 800 MeV (p, p') work.¹⁸

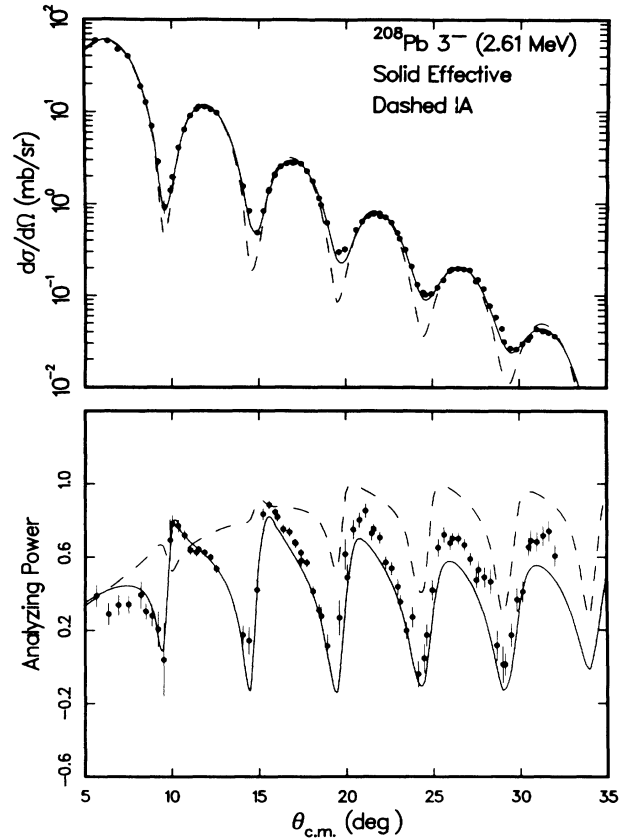


FIG. 16. Differential cross section and analyzing power data for excitation of the 3_1^- (2.61 MeV) state of ^{208}Pb are compared with results of DWBA analysis obtained with the effective interaction (solid curve) and the impulse approximation (dashed curve).

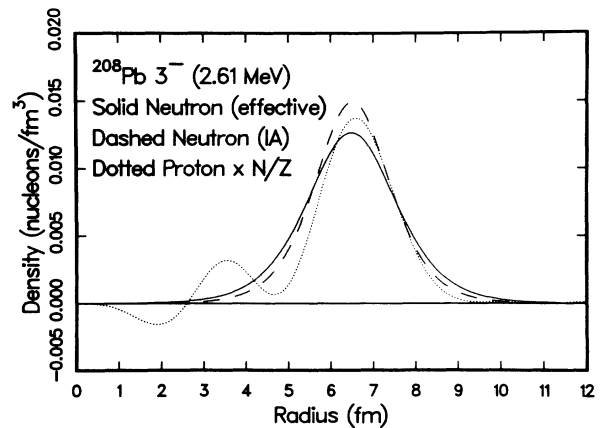


FIG. 17. Model neutron transition densities for the 3_1^- state of ^{208}Pb obtained from the effective interaction analysis (solid curve) and IA analysis (dashed curve) are compared with the renormalized ($\times N/Z$) point-proton transition density (dotted curve) unfolded from the (e, e') results of Ref. 44.

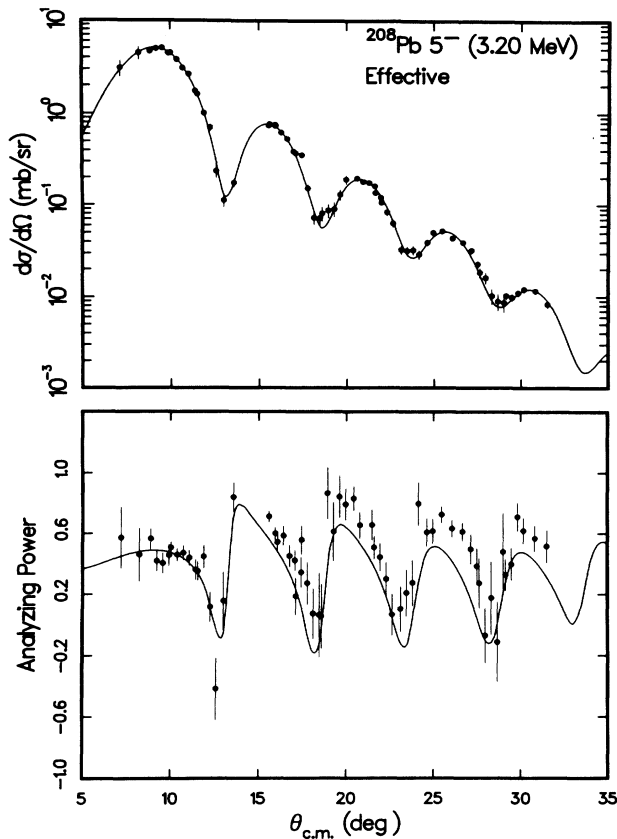


FIG. 18. Same as Fig. 5, except for the 5^- (3.20 MeV) state of ^{208}Pb .

V. SUMMARY AND CONCLUSIONS

We have analyzed new differential cross section and analyzing power angular distribution data for 500 MeV (\bar{p}, p') excitation of low-lying states in $^{40,48}\text{Ca}$, ^{90}Zr , and ^{208}Pb . The analysis used a microscopic DWBA model with effective (EI) or impulse-approximation (IA) proton-nucleon interactions. The EI calculations led to significantly better descriptions of the data than did calculations using the IA.

Estimates of the neutron transition densities in the surface and tail regions were deduced using simple, model-dependent forms. For the effective interaction analysis the results obtained for the low-lying ^{40}Ca isoscalar excitations indicate that the deduced structure information obtained with the EI is sensible, based on a comparison with known proton transition densities. The multipole

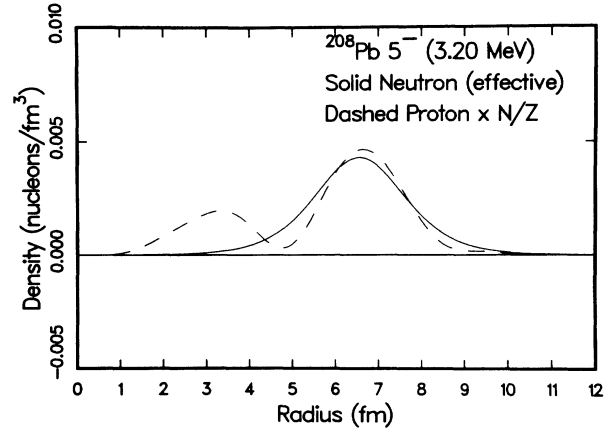


FIG. 19. Same as Fig. 9, except for the 5^- state of ^{208}Pb and a point-proton density derived from results in Ref. 44.

moments deduced from the EI analysis of the other data are in overall agreement with previous results with the exception of those for the low-lying states of ^{90}Zr . The result of the analysis indicate that the 500 MeV effective interaction provides very good descriptions of 500 MeV (\bar{p}, p') data and should be useful in further studies of proton-nucleus scattering at and near this energy which are aimed at the determination of nuclear structure information.

Optical potential ambiguities in the calculation of the distorted waves were investigated by means of the Schrödinger equivalent optical potential (generated from Lorentz scalar and timelike vector optical potentials used in Dirac equation descriptions of the elastic observables). The uncertainty in deduced nuclear structure information from analysis of 500 MeV (\bar{p}, p') data was shown to be potentially large due to such ambiguities. Conversely, knowledge of the structure for a particular excitation, such as isoscalar excitations in self-conjugate nuclei, should permit a simultaneous analysis of the elastic and inelastic scattering data to resolve such ambiguities. The ^{40}Ca data should be especially useful for this purpose. Hopefully, such a study will be made in the future.

ACKNOWLEDGMENTS

The authors thank J. McGill, R. Ferguson, Kamal K. Seth, D. Barlow, A. Saha, S. Iverson, M. Kaletka, M. Bosko, and D. Smith for help during the experiment. We also thank M. Franey for assistance with the theoretical analysis. This work was supported by the U.S. Department of Energy and The Robert A. Welch Foundation.

¹M. L. Barlett, W. R. Coker, G. W. Hoffmann, and L. Ray, Phys. Rev. C **29**, 1407 (1984).

²G. W. Hoffmann *et al.*, Phys. Rev. Lett. **47**, 1436 (1981).

³A. Rahbar *et al.*, Phys. Rev. Lett. **47**, 1811 (1981).

⁴B. Aas *et al.*, Bull. Am. Phys. Soc. **26**, 1125 (1981), and private communication.

⁵A. K. Kerman, H. McManus, and R. M. Thaler, Ann. Phys.

(N.Y.) **8**, 551 (1959).

⁶K. K. Seth *et al.*, Phys. Lett. **158B**, 23 (1985).

⁷L. E. Smith, computer program LOAF (unpublished).

⁸I. Sick *et al.*, Phys. Lett. **88B**, 245 (1979); J. B. Bellicard *et al.*, Phys. Rev. Lett. **19**, 527 (1967); J. Heisenberg *et al.*, Phys. Rev. C **29**, 97 (1984), and private communication; B. Frois *et al.*, Phys. Rev. Lett. **38**, 152 (1977).

- ⁹R. A. Arndt *et al.*, Phys. Rev. D **28**, 97 (1983), and private communication.
- ¹⁰J. A. McNeil, L. Ray, and S. J. Wallace, Phys. Rev. C **27**, 2123 (1983).
- ¹¹G. R. Satchler, Nucl. Phys. **55**, 1 (1964).
- ¹²R. Schaeffer and J. Raynal, computer program DWBA-70 (unpublished); J. Raynal, Nucl. Phys. **A97**, 572 (1967), modified by M. A. Franey and W. G. Love.
- ¹³J. Carr, F. Petrovich, and J. Kelly, computer program ALLWORLD (unpublished).
- ¹⁴L. Ray and G. W. Hoffmann, Phys. Rev. C **27**, 2133 (1983).
- ¹⁵B. J. Verhaar, W. C. Hermans, and J. Oberski, Nucl. Phys. **A195**, 379 (1972); H. Sherif and J. S. Blair, Phys. Lett. **26B**, 489 (1968).
- ¹⁶K. K. Seth, in *Proceedings of the International Symposium on Electromagnetic Properties of Atomic Nuclei* (Tokyo Institute of Technology, Tokyo, 1984), pp. 54–76; K. K. Seth, private communication.
- ¹⁷R. A. Eisenstein, D. W. Madsen, H. Theissen, L. S. Cardman, and C. K. Bockelman, Phys. Rev. **188**, 1815 (1969).
- ¹⁸M. M. Gazzaly *et al.*, Phys. Rev. C **25**, 408 (1982).
- ¹⁹G. S. Adams *et al.*, Phys. Rev. C **21**, 2485 (1980).
- ²⁰E. Bleszynski *et al.*, Phys. Rev. C **25**, 2563 (1982).
- ²¹A. Chaumeaux, V. Layly, and R. Schaeffer, Ann. Phys. (N.Y.) **116**, 247 (1978).
- ²²K. G. Boyer *et al.*, Phys. Rev. C **29**, 182 (1984).
- ²³C. L. Morris *et al.*, Phys. Rev. C **24**, 231 (1981).
- ²⁴P. M. Endt and C. Van Der Leun, Nucl. Phys. **A310**, 533 (1978), and references therein.
- ²⁵M. L. Barlett, G. W. Hoffmann, and L. Ray, Phys. Lett. **158B**, 289 (1985).
- ²⁶B. Aas *et al.*, Phys. Rev. C **26**, 1770 (1982).
- ²⁷Herein our reference to “large” or “small” isovector contributions to the excitation means that $\rho_{h,l}^{\text{tran}}(r) - (N/Z)\rho_{p,l}^{\text{tran}}(r)$ is or is not significant in size with respect to $\rho_{p,l}^{\text{tran}}(r)$, respectively. The isovector part of the spin-independent optical potential and the inelastic transition potential for these low-lying, collective states is always very small compared to the isoscalar portion owing to the isoscalar dominance of the two-nucleon spin-independent interaction.
- ²⁸J. A. Carr, F. Petrovich, and J. J. Kelly, in *Neutron-Nucleus Collisions—A Probe of Nuclear Structure*, in Proceedings of the International Conference at Burr Oak State Park, Ohio, AIP Conf. Proc. No. 124, edited by J. Rapaport, R. W. Finlay, S. M. Grimes, and F. S. Dietrich (AIP, New York, 1985), pp. 230–255.
- ²⁹J. J. Kelly, submitted to Phys. Rev. C.
- ³⁰W. R. Coker, J. D. Lumpe, and L. Ray, Phys. Rev. C **31**, 1412 (1985).
- ³¹J. R. Shepard, J. A. McNeil, and S. J. Wallace, Phys. Rev. Lett. **50**, 1443 (1983).
- ³²B. C. Clark, S. Hama, R. L. Mercer, L. Ray, and B. D. Serot, Phys. Rev. Lett. **50**, 1644 (1983).
- ³³B. C. Clark *et al.*, Phys. Rev. C **28**, 1421 (1983).
- ³⁴L. G. Arnold, B. C. Clark, R. L. Mercer, and P. Schwandt, Phys. Rev. C **23**, 1949 (1981).
- ³⁵B. C. Clark, R. L. Mercer, and P. Schwandt, Phys. Lett. **122B**, 211 (1983).
- ³⁶J. A. McNeil, J. R. Shepard, and S. J. Wallace, Phys. Rev. Lett. **50**, 1439 (1983).
- ³⁷L. Ray and G. W. Hoffmann, Phys. Rev. C **31**, 538 (1985).
- ³⁸B. C. Clark, in *Medium Energy Nucleon and Antinucleon Scattering*, Vol. 243 of *Lecture Notes in Physics*, edited by H. V. von Geramb (Springer-Verlag, Berlin, 1985), pp. 391–412.
- ³⁹J. Wise *et al.*, Phys. Rev. C **31**, 1699 (1985); J. Wise, Ph.D. dissertation, University of Virginia, 1982 (unpublished); J. Wise, private communication.
- ⁴⁰K. G. Boyer *et al.*, Phys. Rev. C **24**, 598 (1981).
- ⁴¹N. J. DiGiacomo *et al.*, Phys. Rev. C **19**, 1132 (1979).
- ⁴²M. M. Gazzaly *et al.*, Phys. Rev. C **28**, 294 (1983).
- ⁴³O. Schwentker *et al.*, Phys. Rev. Lett. **50**, 15 (1983).
- ⁴⁴J. Heisenberg, J. Lichtenstadt, C. N. Papanicolas, and J. S. McCarthy, Phys. Rev. C **25**, 2292 (1982); J. Heisenberg, private communication; J. Lichtenstadt, Ph.D. dissertation, Massachusetts Institute of Technology, 1979 (unpublished).
- ⁴⁵D. Goutte *et al.*, Phys. Rev. Lett. **45**, 1618 (1980).
- ⁴⁶C. Olmer *et al.*, Phys. Rev. C **21**, 254 (1980).
- ⁴⁷C. Djalali, N. Marty, M. Morlet, and A. Willis, Nucl. Phys. **A380**, 42 (1982).
- ⁴⁸C. N. Papanicolas *et al.*, Phys. Lett. **108B**, 279 (1982).